PEFC Electrode with Enhanced Three-Phase Contact and Built-In Supercapacitive Behavior

G. Selvarani,[a] A. K. Sahu,[a] G. V. M. Kiruthika,[a] P. Sridhar,[a,*] S. Pitchumani,[a] and A. K. Shukla[a,b,*,z]

[a]*Central Electrochemical Research Institute, Karaikudi-630006, India*
[b]*Solid State and Structural Chemistry Unit, Indian Institute of Science, Bangalore-560 012, India*

Hydrous ruthenium oxide, which exhibits both protonic and electronic conduction, is incorporated in the cathode electrocatalyst layer of the membrane electrode assembly for polymer electrolyte fuel cells (PEFCs). The supercapacitive behavior of ruthenium oxide helps realize a fuel cell–supercapacitor hybrid. Platinum (Pt) nanoparticles are deposited onto carbon-supported hydrous ruthenium oxide and the resulting electrocatalyst is subjected to both physical and electrochemical characterization. Powder X-ray diffraction and transmission electron microscopy reflect the hydrous ruthenium oxide to be amorphous and well-dispersed onto the catalyst. X-ray photoelectron spectroscopy data confirm that the oxidation state of ruthenium in Pt anchored on carbon-supported hydrous ruthenium oxide is Ru^{4+}. Electrochemical studies, namely cyclic voltammetry, cell polarization, intrinsic proton conductivity, and impedance measurements, suggest that the proton-conducting nature of hydrous ruthenium oxide helps extend the three-phase boundary in the catalyst layer, which facilitates improvement in performance of the PEFC. The aforesaid PEFC operating with hydrogen fuel and oxygen as oxidant shows a higher power density (0.62 W/cm^2 @ 0.6 V) in relation to the PEFC comprising carbon-supported Pt electrodes (0.4 W/cm^2 @ 0.6 V). Potential square-wave voltammetry study corroborates that the supercapacitive behavior of hydrous ruthenium oxide helps ameliorate the pulse-power output of the fuel cell.
© 2008 The Electrochemical Society. [DOI: 10.1149/1.3005965] All rights reserved.

In the postoil energy economy, hydrogen-based fuel cells are being perceived as a possible energy alternative. Hydrogen-based polymer electrolyte fuel cells (PEFCs) are most promising as they offer an order of magnitude higher power density than any other fuel cell system. A PEFC is fed with hydrogen, which is oxidized at the anode and oxygen that is reduced at the cathode. The protons released during the oxidation of hydrogen pass through the proton exchange membrane to the cathode. The electrons released during the oxidation of hydrogen travel through the external electric circuit, generating an electric current. Owing to the high degree of irreversibility of the oxygen reduction, even under open-circuit condition, the overpotential of the oxygen electrode in a PEFC happens to be about 0.2 V. This represents a loss of about 20% from the theoretical maximum efficiency for a PEFC. Accordingly, the PEFC cathode electrocatalyst has to possess a high intrinsic activity for the electrochemical reduction of oxygen at the cathode in order to attain the maximum efficiency of the PEFC.[1,2]

The activity of the cathode catalyst is reportedly improved by design of the tailored catalyst with controlled composition and microstructure. Nevertheless, the high activity of the catalyst itself is necessary, but not a sufficient condition for good fuel cell performance. To ensure the optimum conditions for effective catalyst utilization, an environment must be provided that allows for an adequate supply of reactants as well as good connectivity of the active sites to the electron and ion-conducting phases. The lack of any of the aforesaid requirements will lead to a decrease in fuel cell performance.[3-6]

Conventionally, to extend the ion-conducting path in the catalyst layer, the electrocatalyst needs to be dispersed with a proton-conducting substance, such as Nafion. This has been shown to improve the performance of the PEFCs, but the platinum in the catalyst layer remains not fully utilized. Besides, Nafion often affects the efficiency of the platinum electrocatalyst by blocking the active sites, restricting the gas permeability of the catalyst layer as well as its electronic conductivity.[6,7] Hence, there is a limit on the quantity of Nafion that needs to be added without affecting the cell performance. Furthermore, it is known that the quite rigid backbone of the Nafion polymer is not able to penetrate into the small microspores. Therefore, the catalyst situated in these microspores will have no connectivity with the proton-conducting phase, and will conse-

quently remain electrochemically inactive. In recent years,[8-10] certain new approaches, such as the introduction of proton-conducting agents in the catalyst layer or catalyst carbon support, have been adopted to further the performance of PEFCs. However, a higher loading of proton-conducting agents in the catalyst layer leads to a decrease in electron conductivity as well as flooding of the electrode.

Hydrous ruthenium oxide ($RuO_2 \cdot xH_2O$) is reported to be a mixed (electron and proton) conductor, making it a potential material for fuel cells. Hydrous ruthenium oxide is also a known material in pseudocapacitors, because it has a high stability, high specific capacitance, and rapid faradaic reaction. However, to improve its utilization, hydrous ruthenium oxide needs to be supported on a high-surface-area carbon.[11,12]

The proton conductive behavior of ruthenium oxide is due to the solid-state surface redox transitions of ruthenium species, schematically written as

$$RuO_x + \delta H^+ + \delta e^- \leftrightarrow RuO_{x-\delta}(OH)_\delta \quad 0 \leqslant \delta \leqslant x \qquad [1]$$
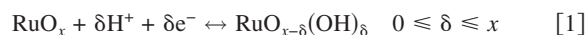
Interestingly, the transitions proceed reversibly over the whole potential region of fuel cell operation.

In the literature,[13-16] a few studies are reported to demonstrate the suitability of hydrous ruthenium oxide as an anode catalyst support for direct methanol fuel cells. Although hydrous ruthenium oxide has been found to increase proton conductivity and catalyst utilization in a membrane electrode assembly (MEA), its influence on the promotion of carbon monoxide and methanol oxidation is limited. In the case of a fuel cell operated with hydrogen and oxygen, Wang et al.[17] reported the incorporation of a supercapacitive ($RuO_2 \cdot xH_2O$) sublayer between the electrocatalyst layer and Nafion membrane. Their study shows a higher peak power than that of a conventional fuel cell system, but the nominal power of the hybrid system is found slightly inferior in relation to the conventional system due to additional proton transport resistance of the supercapacitive layer. D'Souza et al.[18] have also reported that the addition of hydrous ruthenium oxide into the catalyst layer shows a high peak-power performance, but there is little improvement in the steady-state performance of the fuel cell. The reason for not achieving significant steady-state performance could be attributed to the method of preparation, incorporation, and the need for optimizing hydrous ruthenium oxide loading in the catalyst layer. Besides, the aforesaid studies lack in the characterization of hydrous ruthenium oxide and its mechanistic investigation.

* Electrochemical Society Active Member.
z E-mail: akshukla2006@gmail.com

In the present study, hydrous ruthenium oxide is prepared onto the carbon support followed by impregnation of the Pt catalyst. The optimum amount of ruthenium oxide loading in the cathode catalyst layer is determined through cyclic voltammetry (CV) and cell polarization measurements. Cell polarization, intrinsic proton conductivity, and impedance studies show that the hydrous ruthenium oxide incorporated fuel cell exhibits a superior performance in relation to fuel cell employing carbon-supported platinum electrodes. Furthermore, the capacitance and potential square-wave voltammetry studies show that the hydrous ruthenium oxide incorporated fuel cell possesses a high-energy storage capacity, which helps to improve the pulse power of the fuel cell system.

Experimental

Preparation of hydrous ruthenium oxide.— A chemical route reported elsewhere[11] was adopted to prepare hydrous ruthenium oxide. In brief, $RuCl_3 \cdot xH_2O$ (Alfa Aesar) was dissolved in equal volumes of water and methanol under ultrasonication for 1 h to form organometallic species at room temperature. 0.1 M NaOH solution was then added to the solution with continued mechanical stirring until a pH value 7 was attained to form a turbid suspension of ruthenium oxide. The ruthenium oxide suspension was centrifuged and washed copiously with deionized water until no residual chloride was observed. The ruthenium oxide thus obtained was dispersed in aqueous ammoniacal solution and sonicated for 2 h to form a metastable colloidal solution of $RuO_2 \cdot xH_2O$. To prepare the carbon-supported $RuO_2 \cdot xH_2O$, the required amount of colloidal solution of $RuO_2 \cdot xH_2O$ and carbon were ultrasonicated for 1 h, and the resultant mixture was heated at 60°C in vacuum to remove the solvent. Finally, the carbon-supported ruthenium oxide was annealed at 150°C in air for 2 h.

Preparation of supported platinum catalyst.— A sulfito-complex route was adopted[9] to anchor 40 wt % (w/o) platinum on carbon. The required amount of carbon-supported hydrous ruthenium oxide was suspended in distilled water and agitated in an ultrasonic water bath (Vibronics, 300 W, 250 kHz) to form a slurry. The required amount of $Na_6Pt(SO_3)_4$ was dissolved in 1 M H_2SO_4 and diluted adequately with distilled water. The solution was added dropwise to the carbon slurry with constant stirring at 80°C followed by the addition of 30% H_2O_2 with the temperature maintained at 80°C. The solution was further stirred for 1 h. Subsequently, platinum on carbon was obtained by adding 10% formic acid solution, which was filtered, washed copiously with hot distilled water, and dried in an air oven at 80°C for 2 h. In the subsequent text, carbon-supported platinum catalyst without ruthenium oxide is referred to as sample 1 and platinum anchored on carbon-supported hydrous ruthenium oxide catalyst is referred to as sample 2.

Fabrication of MEAs.— Both the anode and cathode comprise a backing layer, a gas-diffusion layer, and a reaction layer. A Teflonized [15 w/o poly (tetrafluoroethylene), PTFE] carbon paper (Toray-TGP-H-120) of 0.35 mm thickness was employed as the backing layer in these electrodes. To prepare the gas-diffusion layer, Vulcan-XC72R carbon was suspended in cyclohexane and agitated in an ultrasonic water bath for 30 min. To this, 15 w/o PTFE suspension was added with continuous agitation. The resultant slurry was spread onto a Teflonized carbon paper and sintered in a furnace at 350°C for 30 min. To prepare the catalyst layer, the required amount of the catalyst (samples 1 or 2) was suspended in isopropyl alcohol. The mixture was agitated in an ultrasonic water bath and 30 w/o of Nafion (DuPont) solution was added to it with continuous agitation for 1 h. The resulting ink was coated onto the gas-diffusion layer of the electrode. Both the anode and cathode contain the platinum loading of 0.5 mg cm^{-2} (active area 25 cm^2) that is kept identical for all MEAs. To establish effective contact between the catalyst layer and the polymer electrolyte, a thin layer of Nafion solution (5 w/o) diluted with isopropyl alcohol in 1:1 ratio was spread onto the surface of each electrode. MEAs were obtained by hot-pressing the cathode and anode on either side of a pretreated Nafion-1135 membrane at 60 kg cm^{-2} at 130°C for 3 min.

Electrochemical characterization.— Polarization studies on PEFCs.— MEAs were evaluated using a conventional 25 cm^2 fuel cell fixture with a parallel serpentine flow field machined on graphite plates (M/s Schunk Kohlenstofftechnik GmbH, Germany). After equilibration, the single cells were tested at 60°C with humidified gaseous hydrogen at a flow rate of 1 L per min at the anode and humidified gaseous oxygen at a flow rate of 1 L per min at the cathode at atmospheric pressure. While using air in place of oxygen, the flow rate was kept at 1.5 L/min. Measurements of cell potential as a function of current density were conducted galvanostatically using an LCN100-36 electronic load procured from Bitrode Corporation, U.S.A.

CV measurements: Electrochemical surface-area measurements.— CV measurements were conducted to determine the electrochemical surface area using a potentiostat (Autolab-PGSTAT 30) with its leads for reference and counter electrodes connected to the cell anode, and its lead for working electrode connected to the cell cathode. During the experiment, humidified hydrogen and humidified nitrogen were fed to the anode and cathode, respectively. The voltammograms were recorded after a run time of ~ 1 h. During the first hour, the electrode was cycled between 0 and 1 V at a sweep rate of 50 mV/s to attain stable and reproducible voltammograms. The electrochemical surface area (ESA) of Pt catalyst was estimated from the equation[9]

$$ESA(cm^2/gPt) = Q_H(mC/cm^2)/[0.210(mC/cm^2)$$
$$\times \text{ electrode loading}(gPt/cm^2)] \qquad [2]$$

In Eq. 2, Q_H represents the charge of hydrogen desorption and 210 μC/cm^2 is the charge required to oxidize a monolayer of H_2 on smooth platinum surface.

Capacitance measurements.— CVs were obtained to determine the capacitance of the fuel cell with samples 1 and 2 incorporated cathodes. The capacitance was calculated from the following equation[19]

$$C = (\Delta Q/\Delta V) \qquad [3]$$

In Eq. 3, C is the capacitance, ΔQ is the charge obtained by current integration during the discharge scan, and ΔV is the voltage scan. The capacitance values obtained were converted into gravimetic capacitance by dividing the capacitance values by mass. All voltammograms were recorded between −0.5 and +0.5 V at a scan rate of 5 mV/s. During the experiment humidified nitrogen was fed to both the anode and cathode chambers.

Potential square-wave voltammetry study.— The peak power of the fuel cell with samples 1 and 2 was measured under humidified hydrogen at the anode and air at the cathode or humidified nitrogen on either side using a Solartron analytical model 1480 electrochemical interface, under the pulse voltage condition using potential square-wave voltammetry. The potential was stepped between 0.8 and 0.4 V, and the corresponding current was measured.

Comparison of proton conductivity in catalyst layers of PEFCs.— A proton-conducting composite layer comprising carbon or carbon-supported ruthenium oxide with Nafion solution was inserted between a Nafion membrane and the cathode of PEFCs operating with hydrogen and oxygen, and their performance was examined. The performance of the PEFC employing MEA without the composite layer was also obtained for a comparison, as suggested in the literature.[20] Figure 1a provides the schematic diagram of the fuel cell with the MEA comprising sample 1 as cathode, while Fig. 1b and c represent the fuel cells akin to Fig. 1 but with additional carbon and Nafion solution admixture as the composite layer, and carbon-supported ruthenium oxide with Nafion solution as the composite layer, respectively.

Impedance measurements.— An impedance analyzer (Autolab-PGSTAT 30) was employed to measure the resistance of the MEA at the operating cell voltage of 0.8 V. The reference and counter elec-
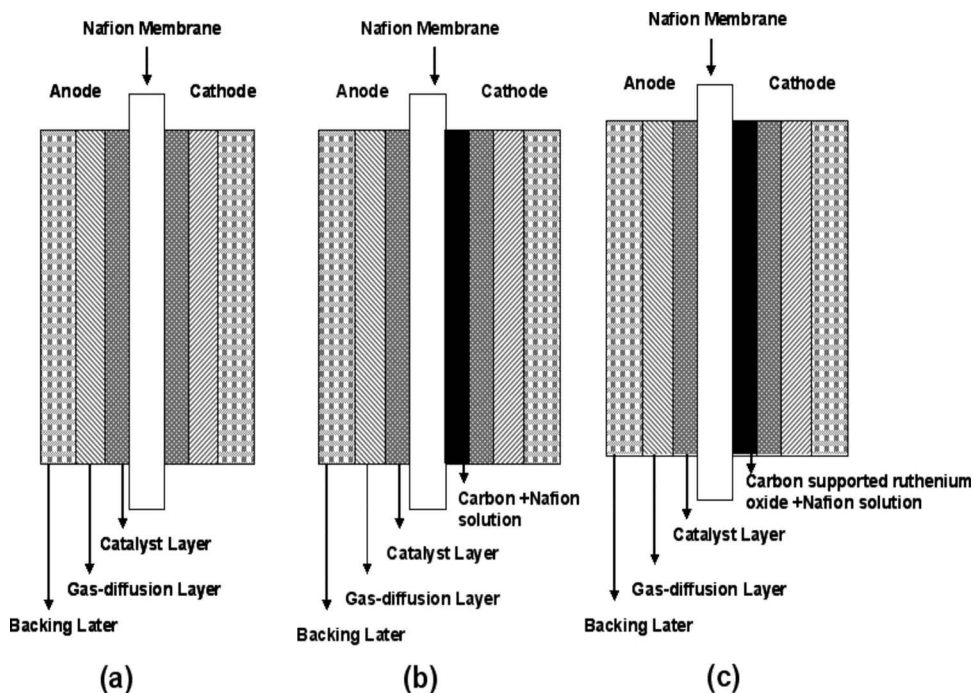
Figure 1. Schematic diagrams of PEFCs with MEAs comprising (a) sample 1 without composite layer, (b) carbon and Nafion solution admixture as composite layer, and (c) carbon-supported ruthenium oxide with Nafion solution admixture as composite layer.

trode leads were connected to the hydrogen electrode, and the working electrode lead was linked to the air electrode. Impedance measurements were conducted in the frequency range between 100 mHz and 5 kHz while imposing a sine wave of 10 mV amplitude.

Physical characterization.— Physical characterization of samples 1 and 2 was carried out using powder X-ray diffraction (XRD) obtained from an X-ray diffractometer (Philips Pan Analytical), and the morphology of ruthenium oxide and platinum was examined through a Tecnai 20 G2 transmission electron microscope (TEM).

X-ray photoelectron spectra (XPS) of the samples were recorded on a MultiLab 2000 (Thermofisher Scientific, UK) fitted with a twin anode X-ray source using Mg Kα radiation (1253.6 eV). For recording the spectrum, the powder samples were pressed onto a conducting carbon tape pasted onto the indium-coated stainless steel stubs. The sample stubs were initially kept in the preparatory chamber overnight to desorb any volatile species at 10^{-9} mbar and were introduced into the analysis chamber having a base pressure of 9.8×10^{-10} mbar for recording the spectra. High-resolution spectra averaged over five scans with a dwell time of 100 ms in steps of 0.02 eV were obtained at a pass energy of 20 eV in constant analyzer energy mode. Experimental data were curve fitted with a Gaussian and Lorentzian mixed product function after subtracting the Shirley background. Spin-orbit splitting and the doublet intensities were fixed as described in the literature.[9] The relative intensity of the species on the surface was estimated from the respective areas of the fitted peaks.

Results and Discussion

The structure of hydrous ruthenium oxide comprises a network of rutilelike clusters with extensions in the subnanometer range for highly hydrated samples, along with physi- and chemisorbed water in its grain-boundary regions. Proton transport is facilitated by the hydrous-grain-boundary regions, while electron transport takes place inside the network of RuO_2 clusters. Although proton conductivity is optimized with high water content, the electron conductivity of these samples happens to be low, as most of the RuO_2 clusters are electronically insulated by the hydrous grain boundaries. As water is removed, the RuO_2 clusters grow in size and the grain-boundary regions become narrower until they eventually lead to the formation of interconnections. It is reported that amorphous ruthenium oxide

with annealing at a critical temperature close to its crystalline temperature ($\sim150°C$) shows optimum protonic and electronic conductivity.[18,19,21] Accordingly, in the present study, hydrous ruthenium oxide annealed at $150°C$ is used.

Powder-XRD patterns for samples 1 and 2 are shown in Fig. 2. Diffraction peaks at ca. 40, 47, and 68° are due to (111), (200), and (220) planes of the face-centered cubic structure for Pt metal, respectively. The XRD peak positions for samples 1 and 2 remain identical, indicating that the modification procedure has little effect on the crystallinity of Pt. An estimation of mean size of Pt in samples 1 and 2 is performed from the half-width at full maximum for the Pt(111) Bragg reflection peak using the Debye–Scherrer equation. The mean particle size of Pt in samples 1 and 2 is 4.2 and 3 nm, respectively. A decrease in particle size is observed in hydrous ruthenium oxide incorporated catalyst, which may be due to the prevention of agglomeration of Pt particles by amorphous hydrous ruthenium oxide. In addition, the XRD experiments are carried out
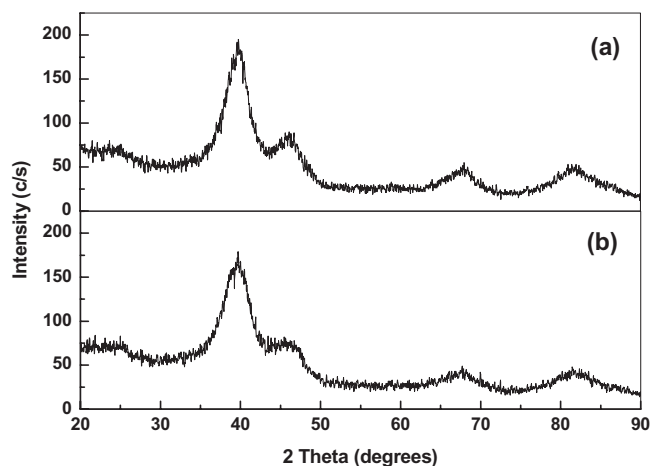

Figure 2. Powder XRD patterns for (a) sample 1 and (b) sample 2 containing 10 w/o hydrous ruthenium oxide.
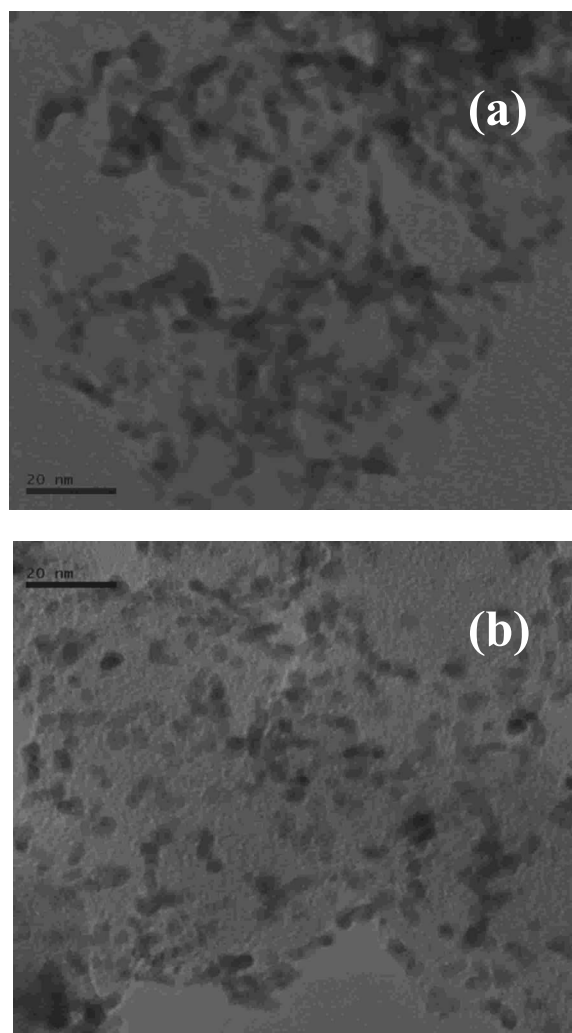
Figure 3. Electron micrographs for (a) sample 1 and (b) sample 2 containing 10 w/o hydrous ruthenium oxide.
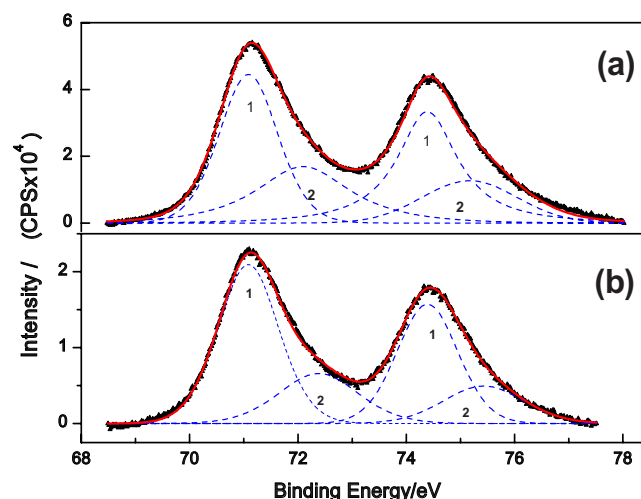

Figure 4. (Color online) XPS spectra for Pt (4f) region in (a) sample 1 and (b) sample 2 containing 10 w/o hydrous ruthenium oxide. The solid line represents the fitted XPS spectra, and broken line represents the peaks due to platinum metal and its oxides (1,2 correspond to Pt^0 and Pt^{2+} species, respectively).

The XPS spectrum of the C (1s) peak entirely covers the Ru $(3d_{3/2})$ and partially overlaps with Ru $(3d_{5/2})$. Hence, a quantitative estimation of the oxidation state of ruthenium is not possible from these spectra.[22] Therefore, the Ru $(3p_{1/2,3/2})$ region has been studied to examine different ruthenium species, and the deconvoluted spectrum of sample 2 is shown in Fig. 5. Spectral parameters obtained from the analysis of the Ru $(3p_{1/2,3/2})$ region are listed in Table II. The main Ru $(3p_{3/2})$ peak in RuO_2, is deconvoluted into a component observed at 463.1 eV and a higher-energy component observed at 465.5 eV, which are ascribed to Ru^{4+} and hydrous Ru^{4+} species, respectively.[24,25] This suggests that the oxidation state of ruthenium in Pt anchored on carbon-supported ruthenium oxide is Ru^{4+}.

The O (1s) spectrum for sample 1 shown in Fig. 6a could be deconvoluted into three components. Peak 1 (530.7 eV) is ascribed to O^{2-} of PtO; peak 2 (532.3 eV) is due to adsorbed OH-species, and peak 3 (533.8 eV) is due to physisorbed water.[26-28] The O (1s) spectrum for sample 2 shown in Fig. 6b could be deconvoluted into five components. Peaks 1, 2, and 3 are similar to sample 1 but for the higher intensity for peak 3 in sample 2; peaks 4 (529.1 eV) and 5 (535.3 eV) are due to O^{2-} in RuO_2 and free water, respectively.[29,30] The presence of higher-intensity peaks 3 and 5 in sample 2 clearly reflects the hydrated nature of sample 2.

The enhanced catalytic nature of the fuel cell with hydrous ruthenium incorporated cathode is further examined through CV, polarization, and impedance studies. CV studies are carried out to quantify the variation of ESA and percentage of platinum utilization with varying hydrous ruthenium oxide loading in sample 2 and compared with sample 1. A typical CV is shown in Fig. 7. The peak between 0.0 and 0.4 V provides the information on the hydrogen

for hydrous ruthenium oxide without carbon support, with carbon support, and after annealing at 150°C. These XRD patterns are akin to that reported in the literature.[14,16,19]

TEM images for samples 1 and 2 are shown in Fig. 3a and b. In Fig. 3a, it is seen that the nanometer-sized Pt particles are not in proper shape and less homogeneously dispersed throughout the catalyst. Figure 3b shows the TEM image for sample 2. Amorphous ruthenium oxide is barely visible due to the high platinum loading on carbon. However, platinum is homogeneously dispersed on carbon. In addition, the size of the Pt particle is smaller than that in sample 1.

Figure 4 shows XPS Pt (4f) core level region for samples 1 and 2. Pt (4f) regions for samples 1 and 2 can be fitted into two sets of spin-orbit doublets. For sample 1, the Pt $(4f_{7/2,5/2})$ peaks at 71.09, 72.10 eV and 74.39, 75.17 eV have been assigned to Pt^0 and Pt^{2+}, respectively.[9,22,23] The full-width at half-maximum (fwhm) values for Pt^0 and Pt^{2+} peaks are 1.33 and 2.06 eV. Pt $(4f_{7/2,5/2})$ peaks for sample 2 at 71.09, 72.38 eV and 74.39, 75.43 eV have been assigned to Pt^0 and Pt^{2+}, respectively, and their corresponding fwhm's are 1.37 and 2.13 eV. The relative intensities of the different species obtained from the respective area are shown in Table I. Pt^0 is found to be the predominant species in both samples 1 and 2. The Pt^0 percentage in sample 2 is 77, which is higher than its value in sample 1 (60%). This is due to the oxophilic nature of ruthenium in sample 1.[22]

Table I. Binding energy (BE), fwhm, and relative intensity values for different Pt species as observed from Pt (4f) spectra for sample 1 and sample 2.

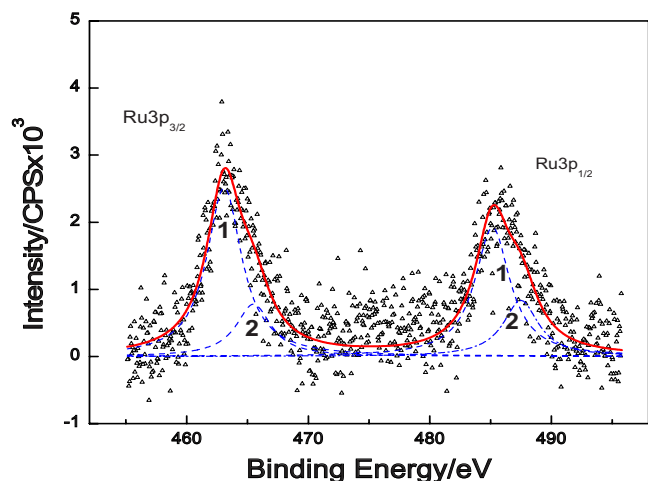| Catalyst | Pt species | BE (eV) | | fwhm (eV) | Relative intensity (%) |
		$4f_{7/2}$	$4f_{5/2}$		
Sample 1	Pt^0	71.09	74.39	1.33	60
	Pt^{2+}	72.1	75.17	2.06	40
Sample 2	Pt^0	71.09	74.39	1.37	77
	Pt^{2+}	72.38	75.43	1.81	23

Figure 5. (Color online) XPS spectra for Ru (3p) region for sample 2 containing 10 w/o hydrous ruthenium oxide. The solid line represents the fitted XPS spectra, and broken line represents the peaks due to ruthenium (IV) oxides (1,2 correspond to RuO_2 and $RuO_2 \cdot xH_2O$, respectively).

Figure 7. (Color online) CVs for samples 1 and 2 with varying amounts of hydrous ruthenium oxide (25 cm^2 single cell at 25°C; N_2 and H_2 streams at cathode and anode, respectively; scan rate = 50 mV/s).

adsorption/desorption. The coulombic charge for oxidation of hydrogen, corresponding to the area under the anodic peak minus the double-layer charge, increases with increased loading of ruthenium oxide in sample 2 with a maximum at 10 w/o, and subsequently decreases as the ruthenium oxide loading is increased further.

ESA and adsorbed hydrogen charge (Q_H) are calculated from CV data and the results are presented in Table III. An increase in platinum utilization is found after incorporation of hydrous ruthenium oxide onto the carbon support. This is due to the extension of proton and electron conducting paths in the catalyst layer. The optimum loading is found to be 10 w/o in sample 2. However, a further

Table II. BE, fwhm, and relative intensity values for different Ru species as observed from Ru ($3p_{3/2}$) spectra for sample 1.

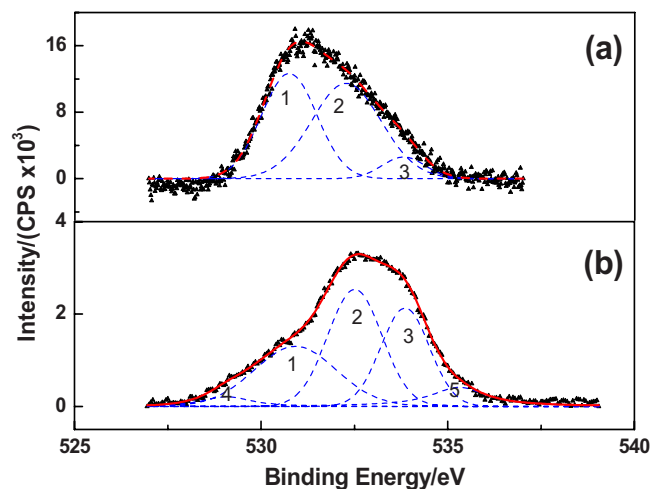| Catalyst	Ru species	BE of Ru ($3p_{3/2}$) (eV)	fwhm (eV)	Relative intensity (%)
Sample 2	RuO_2	463.1	3.45	76
	$RuO_2 \cdot xH_2O$	465.5	3.5	24

Figure 6. (Color online) O (1s) region in (a) sample 1 and (b) sample 2 containing 10 w/o hydrous ruthenium oxide. The solid line represents the fitted XPS spectra, and broken line represents the peaks due to various forms of oxides.
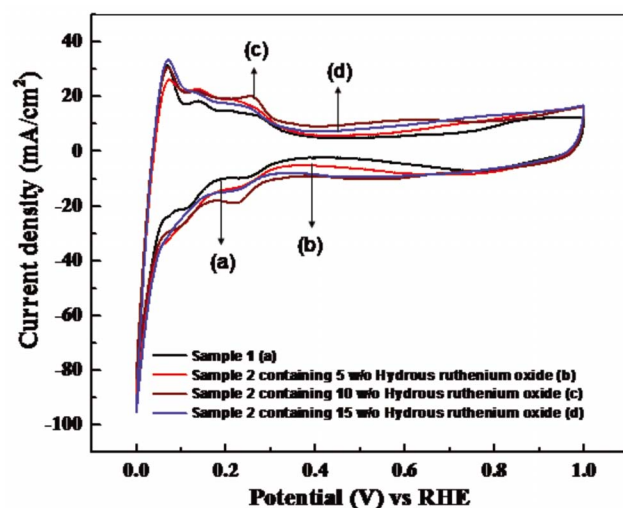
increase in ruthenium oxide loading to 15 w/o decreases Pt utilization, possibly due to the increased hydrophilic nature, which results in reduced mass transport to the catalyst sites.

The potential range of 0.4–0.55 V in CV is responsible for the double-layer charge. The hydrous ruthenium incorporated system shows a higher double-layer charge than the one without it. This is due to the capacitance behavior of hydrous ruthenium oxide.

The capacitive behavior of PEFC containing Pt/C–$RuO_2 \cdot xH_2O$ (10 w/o) electrode is measured using CV in nitrogen environment to investigate the influence of hydrous ruthenium oxide. For clarity, the capacitive behavior of PEFC with Pt/C electrode is also tested under the same conditions. CV curves exhibit pseudocapacitive behavior between −0.5 and +0.5 V. For a comparison, CV curves for fuel cells containing sample 2 (limited to 10 w/o of hydrous ruthenium oxide) and sample 1 are shown in Fig. 8. CVs are recorded at a scan rate of 5 mV/s. The hydrous ruthenium oxide incorporated system exhibits a higher capacitance than the one without it. The superior capacitive performance of the ruthenium incorporated system is due to the pseudocapacitive nature of ruthenium oxide. For the PEFC without hydrous ruthenium oxide, the observed capacitance is attributed to the double-layer capacitance of carbon black that is used as a supporting material for the Pt electrocatalyst.

It is well-known that hydrous ruthenium oxide has a good proton conductivity, high specific power density, rapid charge/discharge behavior, and is capable of sustaining several charge–discharge cycles without any perceptible capacity decay. Hence, the fuel cell catalyst-

Table III. Hydrogen adsorption charge and electrochemical surface area of Pt with different w/o hydrous ruthenium oxide onto the catalyst-carbon support.

Catalyst	Q_H^a (mC)	ESA^b (m^2/g of Pt)
Sample 1	66.30	63.1
Sample 2 with 5 w/o hydrous ruthenium oxide	74.04	70.5
Sample 2 with 10 w/o hydrous ruthenium oxide	80.58	76.7
Sample 2 with 15 w/o hydrous ruthenium oxide	72.69	69.3

[a] Q_H: Experimentally determined adsorbed hydrogen charge.
[b] ESA: Electrochemically determined active surface area from Q_H assuming 0.210 mC/cm^2 for Q_H on smooth platinum.
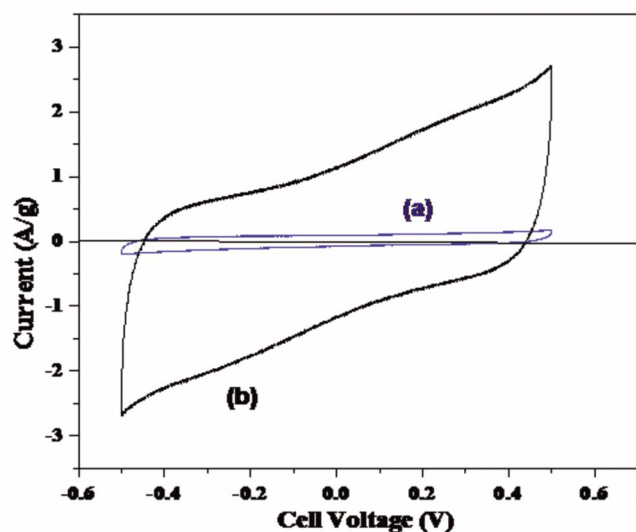
Figure 8. (Color online) CVs for PEFCs with (a) sample 1 and (b) sample 2 containing 10 w/o hydrous ruthenium oxide (scan rate: 5 mV/s in nitrogen atmosphere).

Figure 10. (Color online) Steady-state performance of PEFC (H_2-air) (a) sample 1 and (b) sample 2 containing 10 w/o hydrous ruthenium oxide.

containing ruthenium oxide cathode is expected to have a high steady-state performance and peak-power output due to the high-capacitive component.

The steady-state performance of the H_2/O_2 PEFCs employing a cathode with sample 2 (5, 10, and 15 w/o hydrous ruthenium oxide) and sample 1 are evaluated from cell polarization data shown in Fig. 9. It can be seen that the cell comprising the hydrous ruthenium oxide incorporated cathode catalyst performs better in relation to the cell without the hydrous ruthenium oxide catalyst over the entire polarization regime. A maximum power density of 0.62 W/cm² is achieved at 0.6 V with a catalyst having 10 w/o of hydrous ruthenium oxide, which is 35% higher than sample 2 (0.4 W/cm² at 0.6 V). However, the PEFC comprising the cathode with catalyst containing sample 2 with 15 w/o hydrous ruthenium oxide exhibits power densities lower than the PEFCs with cathodes having sample 1 with 10 and 5 w/o of hydrous ruthenium oxide.

A higher amount of hydrous ruthenium oxide in the cathode catalyst layer is expected to increase the utilization of platinum by the extension of proton and electron conducting paths. However, the present study indicates that a higher amount of hydrous ruthenium oxide shows a lesser performance. This could be due to the reduced access of the reactant gas to the active sites due to flooding. Thus,
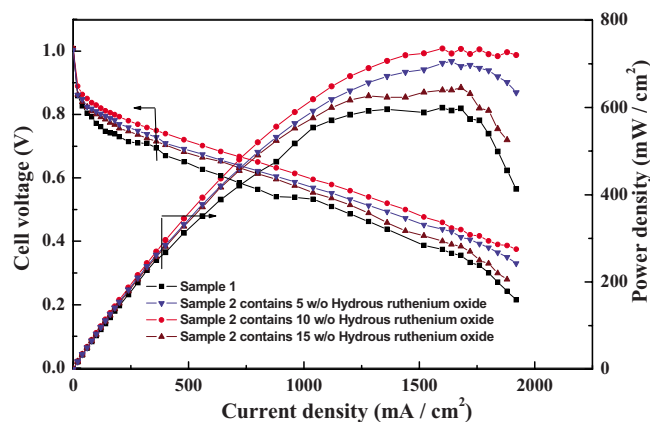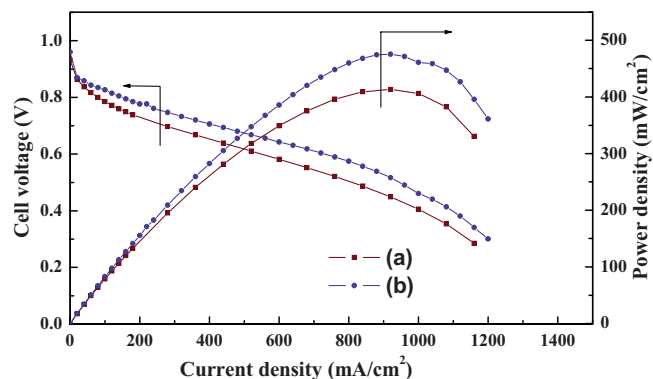
sample 2 having 10 w/o hydrous ruthenium oxide incorporated fuel cell yields an optimum performance with maximum permeability for reactant and catalyst utilization.

The steady-state performance of H_2-air PEFCs comprising a cathode catalyst with sample 2 with 10 w/o hydrous ruthenium oxide and sample 1 is evaluated and the cell polarization data are presented in Fig. 10. The performance of PEFC comprising a cathode catalyst with hydrous ruthenium oxide is superior to the one without it.

Figure 11 shows the galvanostatic performance curves for PEFCs operating with H_2 and O_2 comprising MEAs with and without a proton-conducting composite layer in the electrolyte path between Nafion membrane and the cathode. The performance of the PEFC employing the MEA with a proton-conducting composite layer is found to be inferior in relation to the PEFC employing the MEA without the composite layer. Among the PEFCs employing MEAs comprising a proton-conducting composite layer, the PEFC with carbon-supported hydrous ruthenium oxide with a Nafion solution layer shows a higher performance in relation to the PEFC employing the MEA with a carbon and Nafion solution admixture as the composite layer. The improvement in performance is due to the intrinsic proton conductivity of amorphous $RuO_2 \cdot xH_2O$, as all other parameters, namely carbon and Nafion loadings in the composite layer, cell configuration, and testing conditions are kept identical. This
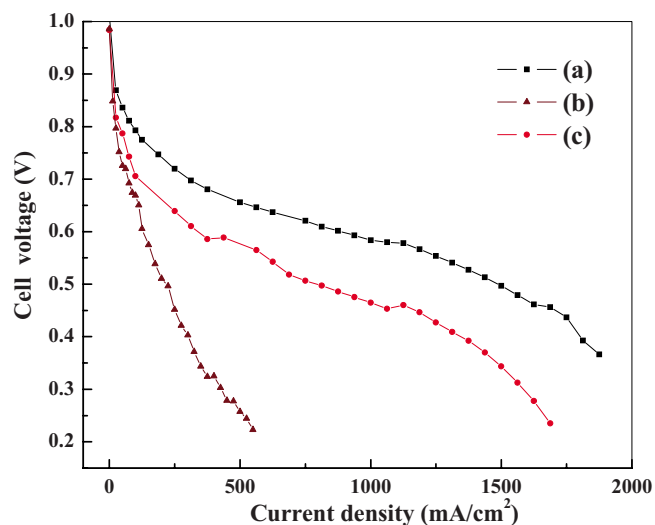

Figure 9. (Color online) Steady-state performance of PEFCs (H_2–O_2) for samples 1 and 2 with varying loading of hydrous ruthenium oxide.

Figure 11. (Color online) Steady-state performance of PEFCs (H_2 and O_2) with MEAs comprising (a) sample 1 without composite layer, (b) carbon and Nafion solution admixture as the composite layer, and (c) carbon-supported ruthenium oxide with Nafion solution as composite layer.
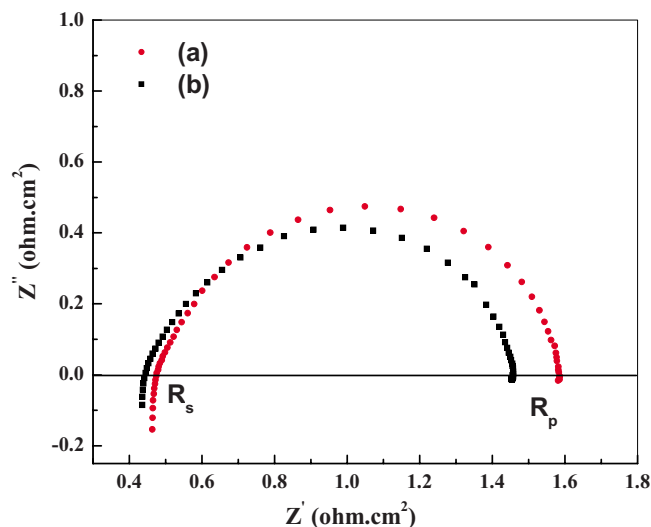
Figure 12. (Color online) Impedance spectrum for PEFCs (H$_2$-air) with the MEA comprising (a) sample 1 and (b) sample 2 containing 10 w/o hydrous ruthenium oxide at 0.8 V.

Figure 14. Peak-power performance of PEFCs comprising cathode (a) sample 1 and (b) sample 2 containing 10 w/o hydrous ruthenium oxide under humidified nitrogen atmosphere.

study suggests that the high proton-conducting nature of hydrous ruthenium oxide extends the proton-conduction path in the catalyst layer. This is in conformity with the findings of Fu et al.[21] on the proton transport properties of RuO$_2$·xH$_2$O by solid-state ^{1}H NMR, wherein it is shown that the activation for proton transport, E_a, in RuO$_2$·xH$_2$O annealed at 150°C is minimal, and increases for RuO$_2$·xH$_2$O annealed at lower or higher temperatures. The lowest E_a value reported for RuO$_2$·xH$_2$O heated at 150°C is ∼2.4 kJ/mole. For comparison, Ye et al.[31] have measured activation energy for proton transport in Nafion using the same solid-state ^{1}H NMR technique. The E_a value of dried Nafion is 16.4 kJ/mole, while that for hydrated Nafion is 11 kJ/mole. The activation energy for proton transport in Nafion is higher than the minimal E_a value of RuO$_2$·xH$_2$O heated at 150°C.

To determine the effect of hydrous ruthenium oxide on the performance of PEFCs, the electrochemical impedance spectra ($Z = Z' + iZ''$) of H$_2$-air cells are recorded at an operating cell voltage of 0.8 V and the data are presented in Fig. 12. The high-frequency intercept with the real axis represents the ionic resistance of the
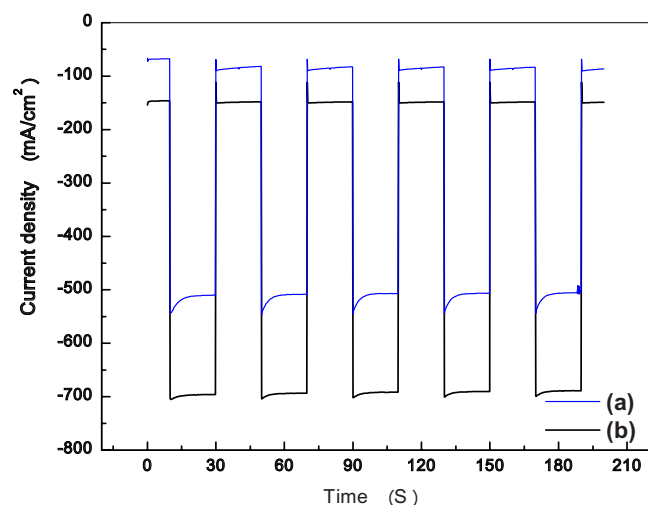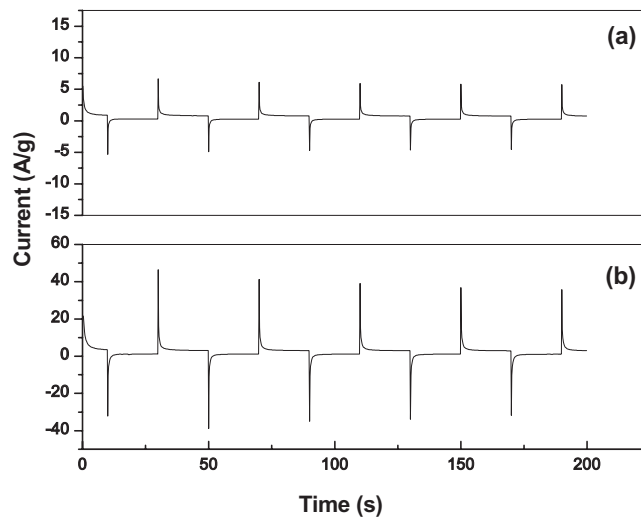

Figure 13. (Color online) Pulse-loading performance of PEFCs with MEAs comprising (a) sample 1 and (b) sample 2 containing 10 w/o hydrous ruthenium oxide using humidified H$_2$-air.

electrolyte (R_s). The impedance spectrum at low frequencies shows a polarization resistance (R_p). The diameter of the semicircle is less in the case of a fuel cell with hydrous ruthenium oxide in the cathode catalyst compared to the one without it, which could be due to the enhanced proton conduction in the catalyst layer.

The square-wave voltammetry performance for H$_2$-air PEFC with sample 2 with 10 w/o hydrous ruthenium oxide and sample 1 is conducted between 0.8 and 0.6 V, and data are presented in Fig. 13. It is seen that the peak, as well as the steady-state current for the PEFC, is increased by the incorporation of hydrous ruthenium oxide in the cathode catalyst layer. This indicates that the discharged supercapacitor element at 0.6 V could be quickly recharged when the operating voltage of the fuel cell jumped back to 0.8 V. Therefore, the discharged supercapacitor element can be recharged effectively during normal fuel cell operation. The increased steady-state performance observed with a hydrous ruthenium oxide incorporated electrode is due to the increased proton conductivity in the catalyst layer.

The peak-power performance of PEFC with sample 2 with 10 w/o hydrous ruthenium oxide and sample 1 is shown in Fig. 14. The peak-power performance study is conducted under humidified nitrogen atmosphere. For the PEFC without hydrous ruthenium oxide cathode, the pulse output is attributed to the double-layer capacitance of carbon black used as a supporting material for Pt electrocatalyst. PEFC with hydrous ruthenium oxide cathode shows a higher peak current than the one with Pt/C. Accordingly, it is conjectured that the rapid reaction kinetics and pseudocapacitance associated with hydrous ruthenium oxide ameliorates the peak current output of PEFC.

Conclusions

The incorporation of hydrous ruthenium oxide onto the carbon support of the platinum catalyst enhances the performance of PEFC. This is achieved by increasing the utilization of Pt by extending the three-phase boundary in the catalyst layer. An optimum loading of hydrous ruthenium oxide (10 w/o) is required to improve the performance of the PEFC. In addition, the supercapacitive behavior of hydrous ruthenium oxide helps improve the pulse power output of the fuel cell.

References

1. J. Larminie and A. Dicks, *Fuel Cell System Explained*, John Wiley & Sons, London (2003).
2. J. O' M. Bockris and S. Srinivasan, *Fuel Cells: Their Electrochemistry*, McGraw-Hill, New York (1969).
3. A. M. Kannan, L. Cindrella, and L. Munukutla, *Electrochim. Acta*, **53**, 2416 (2008).
4. Y. Song, Y. Wei, H. Xu, M. Williams, Y. Liu, L. J. Bonville, H. R. Kunz, and J. M. Fenton, *J. Power Sources*, **141**, 250 (2005).
5. G. A. Rimbu, C. L. Jackson and K. Scott, *J. Optoelectron. Adv. Mater.*, **8**, 611 (2006).
6. S. J. Lee, S. Mukerjee, J. Mc Breen, Y. W. Rho, Y. T. Kho, and T. H. Lee, *Electrochim. Acta*, **43**, 3693 (1998).
7. E. Antolini, L. Giorgi, A. Pozio, and E. Passalacqua, *J. Power Sources*, **77**, 136 (1999).
8. A. P. Saab, F. H. Farzone, and T. A. Zawodzinski, *J. Electrochem. Soc.*, **150**, A214 (2003).
9. G. Selvarani, A. K. Sahu, N. A. Choudhury, P. Sridhar, S. Pitchumani, and A. K. Shukla, *Electrochim. Acta*, **52**, 4871 (2007).
10. J. Maruyama and I. Abe, *J. Electrochem. Soc.*, **151**, A447 (2004).
11. C. C. Hu, W. C. Chen, and K.-H. Chang, *J. Electrochem. Soc.*, **151**, A281 (2004).
12. Y. Zhao, L. Liu, J. Xu, J. Yang, M. Yan, and Z. Jiang, *J. Solid State Electrochem.*, **11**, 283 (2007).
13. F. Scheiba, M. Scholz, L. Cao, R. Schafranek, C. Roth, C. Cremers, X. Qiu, U. Stimming, and H. Fuess, *Fuel Cells*, **6**, 439 (2006).
14. K. Lash, G. Hayn, L. Jorissen, J. Garche, and O. Besenhardt, *J. Power Sources*, **105**, 355 (2002).
15. Z. Chen, X. Qiu, B. Lu, S. Zhang, W. Zhu, and L. Chen, *Electrochem. Commun.*, **7**, 593 (2005).
16. D. R. Ralison, P. L. Hagans, K. E. Swider, and J. W. Long, *Langmuir*, **15**, 774 (1999).
17. C. Wang and A. J. Appleby, *J. Electrochem. Soc.*, **150**, A493 (2003).
18. S. R. D'Souza, J. Ma, and C. Wang, *J. Electrochem. Soc.*, **153**, A1795 (2006).
19. A. Foelske, O. Barbieri, M. Hahn, and R. Kotz, *Electrochem. Solid-State Lett.*, **9**, A268 (2006).
20. C. Boyer, S. Gamburzev, O. Velev, S. Srinivasan, and A. J. Appleby, *Electrochim. Acta*, **43**, 3703 (1998).
21. R. Fu, Z. Ma, and J. P. Zheng, *J. Phys. Chem. B*, **106**, 3592 (2002).
22. R. K. Raman, A. K. Shukla, A. Gayen, M. S. Hegde, K. R. Priolkar, P. P. Sarode, and S. Emura, *J. Power Sources*, **157**, 45 (2006).
23. A. K. Shukla, M. K. Ravikumar, A. Roy, S. R. Barman, D. D. Sarma, A. S. Arico, V. Antonucci, L. Pino, and N. Giordano, *J. Electrochem. Soc.*, **141**, 1517 (1994).
24. A. Salomonsson, R. M. Petoral, K. Uvda, C. Aulin, P. K. Ojamae, M. Strand, M. Sanati, and A. L. Spetz, *J. Nanopart. Res.*, **8**, 899 (2006).
25. E. G. Franco and M. Linardi, *Rev. Acad. Cienc. Exactas, Fis., Quim. Nat. Zaragoza*, **11**, 89 (2005).
26. T. L. Barr, *J. Phys. Chem.*, **82**, 1801 (1978).
27. C. Jones and E. Sammann, *Carbon*, **28**, 509 (1990).
28. B. Stypula and J. Stoch, *Corros. Sci.*, **36**, 2159 (1994).
29. D. Briggs and M. P. Seah, *Practical Surface Analysis*, p. 150, John Wiley & Sons, London (1993).
30. C. S. K. Singamsetty, C. U. Pittman, G. L. Booth, G. He, and S. D. Gardner, *Carbon*, **33**, 587 (1995).
31. G. Ye, N. Janzen, and G. R. Goward, *Macromolecules*, **39**, 3283 (2006).